

# Strong interplay between polar and structural topologies

Received: 20 January 2026

Accepted: 23 February 2026

Published online: 13 March 2026

Check for updates

Ru-Jian Jiang<sup>1,2,11</sup>, Mei-Xiong Zhu<sup>1,2,11</sup>, Su-Zhen Liu<sup>1,2</sup>, Yu-Ting Chen<sup>3,4,5</sup>,  
Desheng Ma<sup>6</sup>, Yan-Peng Feng<sup>3,4,7</sup>, Min-Jie Zou<sup>3,4</sup>, Meng-Jiao Han<sup>3,4</sup>,  
Chi Hou Lei<sup>8</sup>, Yu-Jia Wang<sup>1,2</sup>, Yun-Long Tang<sup>1,2</sup>✉, Yin-Lian Zhu<sup>3,4,9</sup>✉ &  
Xiu-Liang Ma<sup>10,3,4,5,7,10</sup>✉

Topological structures in condensed matter systems unlock new possibilities for the development of nanoelectronic devices. However, the potential of antiferroelectrics to host topological features remains largely unexplored, constrained by significant energy barriers from antiparallel dipole coupling that suppress polarization rotation and challenges in high-quality film fabrication. Here for the first time, we find that, dislocations, the most common one-dimensional topological structures in crystals, exhibit unexpectedly strong couplings with polar topologies and induce ordered polar antihedgehog lattices in antiferroelectric PbZrO<sub>3</sub> driven by the interplay of electrostrictive effect and the flexoelectric field. Combined atomic-resolution transmission electron microscopy and phase-field simulations, it is revealed that the polarizations converging at dislocation cores and diverging between dislocations define lattices characterized by checkerboard-like antihedgehogs, respectively. Unexpected interplay between polar and structural topologies establishes a new paradigm for topology design.

For centuries, geometry has provided a precise framework for describing the physical world. The advent of topology, however, has fundamentally transformed condensed matter physics, revealing that phase classification extends beyond the symmetry-based Landau–Ginzburg–Wilson paradigm<sup>1</sup>. By focusing on global invariants rather than local symmetries, topology has introduced a new dimension to phase characterization, enabling the discovery of novel phases with distinct and robust topological signatures. Topological structures in condensed matter systems arise from the intricate interplay among various degrees of freedom, including lattice distortions, charge ordering, spin alignment, and orbital interactions. In

ferroelectric materials, lattice and charge degrees of freedom dominate, unlike in magnetic systems where spin degrees of freedom play the primary role. The coupling of elastic, electrostatic, and gradient energies facilitates the stabilization of exotic topological configurations, including flux-closures<sup>2</sup>, vortices<sup>3</sup>, skyrmions<sup>4</sup>, polar waves<sup>5</sup>, merons<sup>6</sup> and polar Bloch points<sup>7</sup>. Remarkably, the spatial dimensions of ferroelectric topological domains are often orders of magnitude smaller than their magnetic counterparts, positioning them as ideal candidates for next-generation functional electronic devices, particularly in information storage and sensor-driven devices. The discovery of an ever-growing family of ferroelectric topological states continues

<sup>1</sup>Shenyang National Laboratory for Materials Science, Institute of Metal Research, Chinese Academy of Sciences, Shenyang, China. <sup>2</sup>School of Materials Science and Engineering, University of Science and Technology of China, Shenyang, China. <sup>3</sup>Bay Area Center for Electron Microscopy, Songshan Lake Materials Laboratory, Dongguan, China. <sup>4</sup>Dongguan Institute of Materials Science and Technology, Chinese Academy of Sciences, Dongguan, China. <sup>5</sup>Institute of Physics, Chinese Academy of Sciences, Beijing, China. <sup>6</sup>School of Applied and Engineering Physics, Cornell University, Ithaca, NY, USA. <sup>7</sup>Quantum Science Center of Guangdong-HongKong-Macau Greater Bay Area, Shenzhen, China. <sup>8</sup>Department of Physics and Engineering, University of Scranton, Scranton, PA, USA. <sup>9</sup>School of Materials Science and Engineering, Hunan University of Science and Technology, Xiangtan, China. <sup>10</sup>State Key Lab of Advanced Processing and Recycling on Non-ferrous Metals, Lanzhou University of Technology, Lanzhou, China. <sup>11</sup>These authors contributed equally: Ru-Jian Jiang, Mei-Xiong Zhu. ✉e-mail: [yltang@imr.ac.cn](mailto:yltang@imr.ac.cn); [zhuyinlian@sslab.org.cn](mailto:zhuyinlian@sslab.org.cn); [xlma@iphy.ac.cn](mailto:xlma@iphy.ac.cn)

to motivate the exploration of new material platforms, further expanding the landscape of polar topologies and their potential applications.

Research on complex topological structures has predominantly focused on ferroelectric systems for decades. In contrast, antiferroelectrics, as counterparts to ferroelectrics, are distinguished by their inherently zero remnant polarization and field-driven antiferroelectric-ferroelectric phase transitions. Such characteristics render antiferroelectrics highly desirable for high-performance applications, including high-energy storage capacitors<sup>8,9</sup>, memories<sup>10</sup>, cooling devices<sup>11,12</sup>, thermal switches<sup>13</sup>, and electrostrain devices<sup>14,15</sup>. However, the exploration of topological structures in antiferroelectric materials remains largely unexplored, mainly due to two formidable challenges. First, the strong antiparallel dipole coupling in antiferroelectrics, characterized by high switching energy barriers, hinders the control of local polarization rotation and limits effective long-range manipulation under homogeneous external fields. Second, the pronounced mismatch between typical antiferroelectrics, e.g., lead zirconate-based antiferroelectrics, and conventional substrates pose formidable challenges to the fabrication of ultrathin films and superlattices, which serve as critical platforms for topology stabilization and exploration. Nevertheless, recent studies have shown that the unique sensitivity of antiferroelectric order parameters to boundary conditions, strain, electric fields, and temperature enables favorable conditions for polarization rotation<sup>14,16–20</sup>, a key precursor for the stabilization of topological states. The potential realization of topological structures in antiferroelectric materials would complement those observed in ferroelectrics, enriching the understanding of polarization phenomena, and expanding the design possibilities for functional materials. Such topological states could enable functionalities like electric field-driven transformations, offering unprecedented design flexibility and tunability for next-generation high-performance electronic devices and sensors. Despite the exciting prospect of topologies in antiferroelectric materials, the experimental observation of topological textures remains an unresolved challenge.

Here, by using the most common one-dimensional topological structures in crystals, those are, dislocations, we have induced novel polar topological arrays in a classical antiferroelectric material, marking a significant step forward in polar topology research. Specifically, using aberration-corrected scanning transmission electron microscopy (AC-STEM) and phase-field simulations, we report that  $a[0\bar{1}0]$  high-density interfacial dislocation arrays form within the  $\text{PbZrO}_3/\text{KTaO}_3$  (PZO/KTO) heteroepitaxial system to accommodate lattice mismatch. The electrostrictive effect and the flexoelectric field induced by the dislocation network drive the emergence of polar antihedgehog arrays. In these arrays, the combination of polarizations converging at dislocation cores and diverging between dislocations defines a lattice characterized by checkerboard-like antihedgehog. These findings reveal unexpectedly strong couplings between polar and structural topologies, expand the range of materials capable of hosting such structures from ferroelectric to antiferroelectric systems, and provide innovative strategies for designing functional materials.

## Results

### High-density dislocation arrays at heterointerface

High-quality epitaxial PZO thin films were successfully fabricated on (001)-oriented KTO substrates by pulsed laser deposition (PLD) technique. High-resolution X-ray diffraction (HRXRD) confirms the high crystalline quality of the films (Supplementary Fig. 1). The broadening of HRXRD peaks and elongation of the (002) Bragg reflection along the  $Q_z$  direction in reciprocal space maps (RSMs) indicate a continuous changing in the out-of-plane lattice constant (Supplementary Fig. 1 and Supplementary Fig. 2a–2c). Moreover, the (103) reflection reveals the coexistence of strained (S) and relaxed (R) regions, reflecting a distribution of local strain states within the film (Supplementary Fig. 2d–2f). This spatial variation in strain is further corroborated by selected area electron diffraction (SAED) patterns, which exhibit diffuse and elongated diffraction spots (Supplementary Fig. 3), consistent with the presence of multiple strain states in the film.

The cross-sectional TEM dark-field image (Fig. 1a) reveals an array of high-density interfacial dislocations at the PZO/KTO interface,

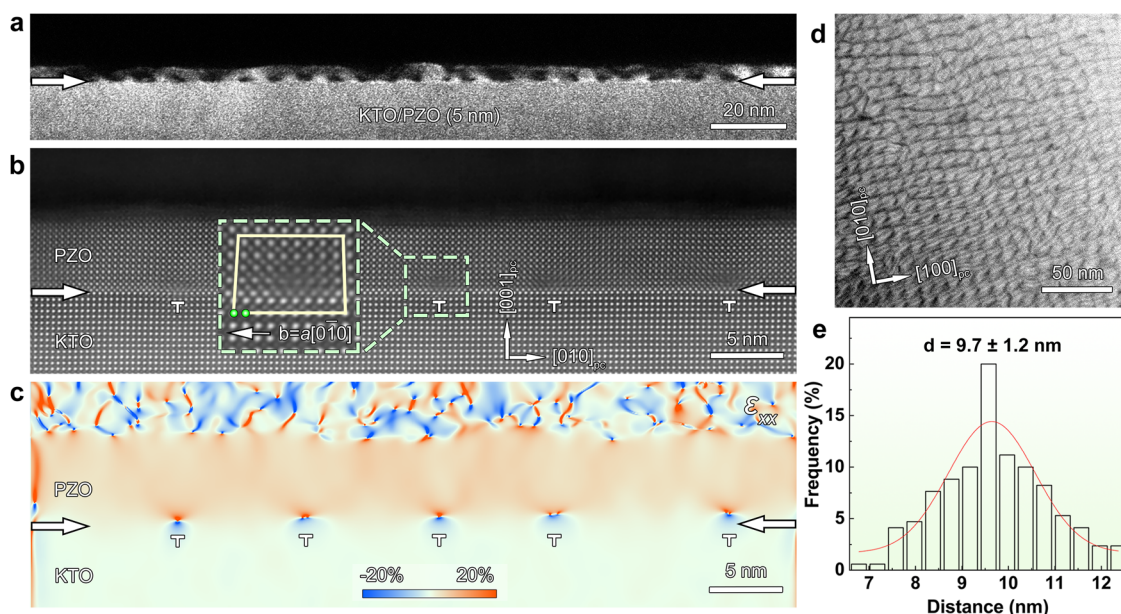


**Fig. 1 | Interfacial dislocations at the PZO/KTO heterointerface.** **a** Large-scale dark-field cross-sectional TEM image of 5 nm PZO film. **b** Low-magnification HAADF-STEM image of the PZO film. The Burgers vector of the dislocation was given in **(b)**. **c** GPA analysis of the  $\epsilon_{xx}$  distributions corresponding to the HAADF-

STEM image in **(b)**. **d** Planar-view BF-STEM image of the dislocation array in PZO film, displaying the interfacial dislocation array more clearly. **e** The statistical distribution of interfacial dislocation spacings in the PZO/KTO film. Positions of the interfacial dislocations near the PZO/KTO interface are indicated by T.

effectively accommodating the large lattice mismatch of 4.2% between the film and the substrate ( $a=3.989$  nm for KTO substrate,  $a_{pc}\approx b_{pc}=4.160$  nm, and  $c_{pc}=4.120$  nm for PZO<sup>21</sup>, where the subscript 'pc' represents pseudo cubic). To further investigate the characteristics of the interfacial dislocations, HAADF-STEM imaging was performed (Fig. 1b) and the Burgers vector of the dislocations was determined as  $\mathbf{b}=a[0\bar{1}0]$ , as shown in the dashed box in Fig. 1b. The in-plane strain ( $\varepsilon_{xx}$ ) distribution, extracted via geometric phase analysis (GPA) and corresponding to Fig. 1b, is shown in Fig. 1c, demonstrating that the dislocations induce a periodic strain field within the film. Further insights into the arrangement of dislocation arrays were obtained from planar TEM observations of a 5 nm PZO film. The planar-view bright field-STEM (BF-STEM) image (Fig. 1d) provides a clear visualization of the dislocation array from an in-plane perspective. Statistical analysis of the dislocation spacing, based on extensive data collection (Fig. 1e), indicates an average spacing of  $9.7\pm 1.2$  nm.

To gain a deeper understanding of the dislocation array, Supplementary Fig. 4 shows the atomic arrangement schematics in PZO/KTO heterostructures from both planar and cross-sectional perspectives. The interfacial dislocation lines are oriented along the  $[100]_{pc}$  and  $[010]_{pc}$  directions at the interface. The two sets of interfacial dislocation lines intersect to form a two-dimensional interfacial dislocation array, as shown in Supplementary Fig. 4.

### Experimental observation of polar antihedgehog domains

Figure 2 shows the atomic-resolved HAADF-STEM image and resolves the strain field and polar topological structure induced by the interfacial dislocations. Detailed analysis of the region above the dislocation core (highlighted by the dashed box in Fig. 2a) was performed from the perspective of lattice distribution. Supplementary Fig. 5 provides definitions for lattice rotation and  $Pb^{2+}$  displacements. Using quantitative analysis based on two-dimensional Gaussian peak fitting, the distributions of the lattice rotation in the horizontal direction ( $R_x$ ) and vertical direction ( $R_y$ ) are obtained in Figs. 2b and 2c, respectively, displaying significant lattice distortions around the high-density dislocations. The  $R_y$  map in Fig. 2c illustrates that lattice rotation distortion decreases gradually from the dislocation core at the interface toward the film surface. To quantitatively visualize this effect, spacing profiles along the  $[00\bar{1}]_{pc}$  direction on both sides of the dislocation core were extracted from the  $R_y$  map (Fig. 2d), revealing a strain gradient exceeding  $10^8\text{ m}^{-1}$  along the  $[00\bar{1}]_{pc}$  direction. Additionally, a similar trend was observed by analyzing the  $R_y$  values over four unit cells above the dislocation core along the  $[010]_{pc}$  direction (Fig. 2e), further confirming the periodic strain distribution and its gradient near the dislocations.

Functional oxides exhibit strong coupling between lattice and charge, where significant lattice distortions near dislocations will strongly affect polarization at the nanoscale<sup>22–29</sup>. To explore the coupling relationship among dislocations, lattice, and polarization, further analysis was conducted. The in-plane (Shift X) and out-of-plane (Shift Y) components of  $\delta_{pb}$ , extracted from the atomic-resolution HAADF-STEM image (highlighted in the dashed box in Fig. 2a), were shown in Supplementary Fig. 6a and 6b, respectively. The Shift X map reveals a periodic positive and negative distribution, with maximum and minimum values adjacent to the dislocation core and an in-plane component that diminishes with increasing distance away from the core, indicating the presence of a polar structure that converges or diverges around the core. In addition, there are periodic distortions between two adjacent dislocations, and the corresponding Shift Y map (Supplementary Fig. 6b) indicates that the displacement directions near the interface and surface are opposite in those regions. The combined observations from the lattice rotation map and  $Pb^{2+}$  displacement map point to the existence of an ordered distributed polar structure strongly coupled to the dislocation array in the 5 nm PZO film.

To reveal the polar structure in the PZO film, polar mapping analysis is performed on atomically resolved HAADF-STEM images (the dashed box in Fig. 2a). The positions of  $Pb^{2+}$  and  $Zr^{4+}$  columns are marked by green and red circles, respectively. Light orange arrows denote the directions of  $\delta_{pb}$  vectors, representing the displacement of  $Pb^{2+}$  cation from the center of its four surrounding  $Zr^{4+}$  columns, and thus indicate the local spontaneous polarization. We performed additional analysis using integrated differential phase contrast STEM (iDPC-STEM), a technique highly sensitive to light elements. This allowed us to directly measure the displacement of Pb cations relative to the geometric center of the oxygen octahedra. The strong agreement between the polarization vectors derived from both methods confirms that  $\delta_{pb}$  is a reasonable method for determining local polarization in our system (Supplementary Note 1 and Supplementary Fig. 7).

The polarization is observed to converge at the core of the dislocations, revealing the presence of ordered polar arrays, as visualized more intuitively in the polarization mapping shown in Fig. 2f. The polarization structure can be decomposed into two basic units, represented by the black and blue dashed boxes (Supplementary Fig. 8). The two units are intertwined rather than spatially separated, with unit at the dislocation core features polarization converging toward the core, reminiscent of center-type domains<sup>30–33</sup>. In contrast, the derived unit situated between adjacent dislocations exhibits a polarization configuration with head-to-head alignment along the out-of-plane  $[001]$  direction and tail-to-tail alignment along the in-plane  $[010]$  direction, forming a cross-like topology characteristic of anti-vortex domains<sup>34–36</sup>. Notably, the centers of the two basic units are not coplanar, a distribution influenced by the strain field generated by the dislocation array. These results provide direct evidence of the strong coupling between the dislocation array and the polar topological structure.

To gain deeper insights into the ordered polar topology from different perspectives, planar samples of 5 nm PZO films were extensively analyzed to complement the cross-sectional observations. An ordered, dot-like contrast in the topography TEM image (Fig. 3a) indicates an ordered structural arrangement in the 5 nm PZO film, which is further supported by the satellite spots in the SAED pattern (Fig. 3b). The spacing between the main and first-order satellite peaks corresponds to a real-space period of  $\sim 10$  nm, this value shows excellent agreement with the average dislocation spacing of  $\sim 9.7$  nm (Fig. 1e). Polarization in dielectric materials is often accompanied with a local polarization field, which can be effectively visualized using differential phase-contrast (DPC) imaging<sup>37</sup>. In the DPC-STEM analysis (Fig. 3c), the  $[100]$  and  $[010]$  directions of the PZO unit cells are aligned with the A-C and B-D segments of the detectors, respectively, as illustrated in the upper-left inset of Fig. 3c. High-resolution DPC-STEM mapping reveals regular modulation of the polarization field across the PZO film, further confirming the ordered nature of the polar topology.

Atomic-resolution HAADF-STEM imaging of the 5 nm PZO film was performed under in-focus conditions to avoid spurious contrast from Moiré patterns, which can arise due to lattice mismatch between the film and substrate (example in Supplementary Fig. 9). The resulting image (Fig. 3d) provides the intrinsic polarization structure. This interpretation is further supported by control experiments on a sample flipped to position the substrate on top (Supplementary Fig. 10). The polarization distribution within one cycle, highlighted in the top-left inset of Fig. 3d, is represented by light orange arrows, which denote the  $\delta_{pb}$  vectors. The convergence centers of the topological structures, identified in the polarization mapping of Fig. 3e (derived from Fig. 3d), are marked with blue circles and reveal an ordered topological lattice. A quantitative analysis of the spacing distribution between these cores indicates a clear ordered arrangement overall,

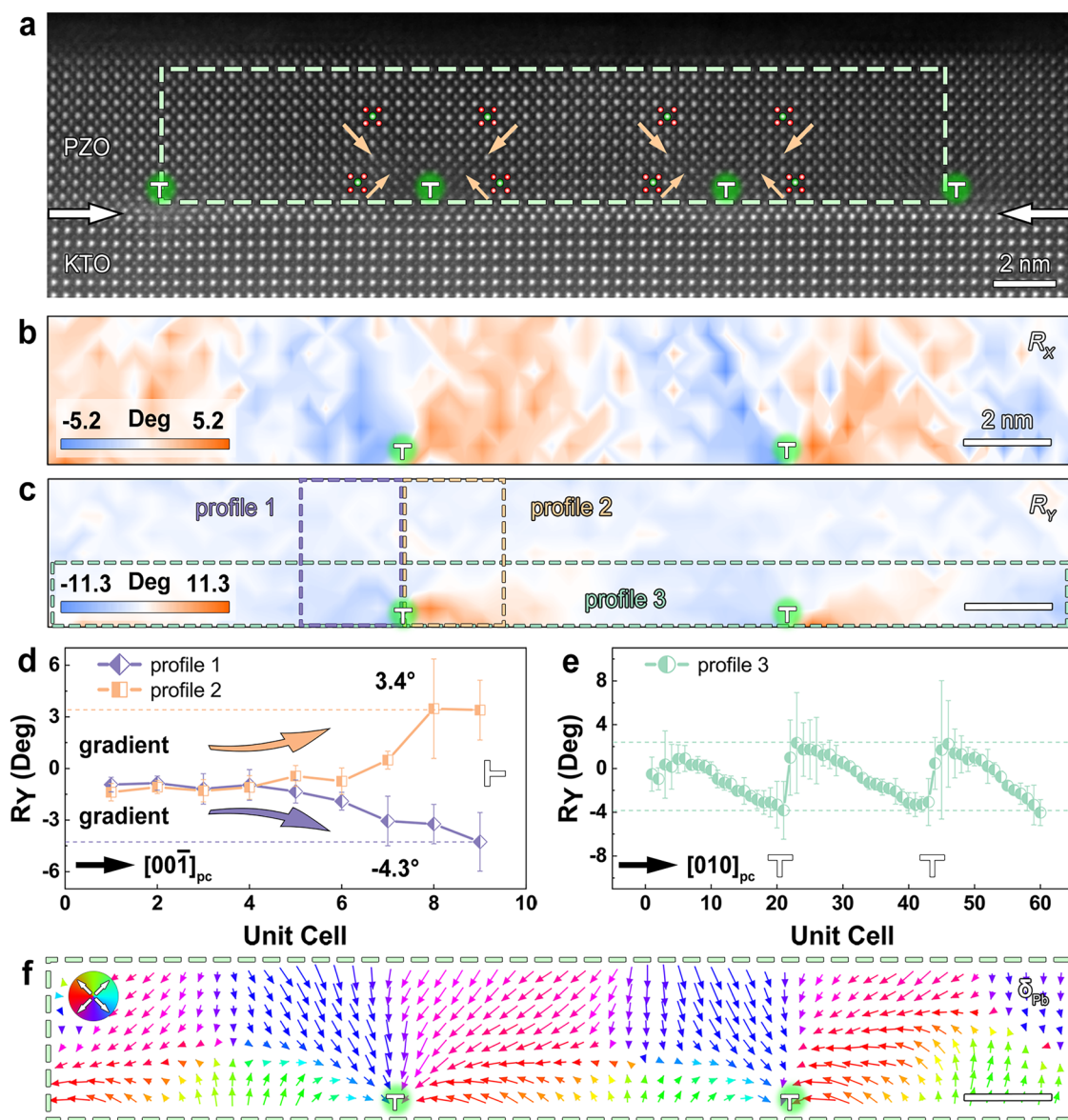


**Fig. 2 | Polar antihedgehogs induced by high-density dislocations.** **a** Atomic-resolved HAADF-STEM image of 5 nm PZO film. The green and red circles denote the position of  $\text{Pb}^{2+}$  and  $\text{Zr}^{4+}$  columns, respectively. The light orange arrows in **(a)** denote  $\text{Pb}^{2+}$  displacement directions. **b** The corresponding  $R_x$  map of the dashed box in **(a)**. **c** The corresponding  $R_y$  map of the dashed box in **(a)**. **d, e** Averaged  $R_y$

spacing profiles for the dashed box in **(c)**, showing the induced  $R_y$  gradients by strain-field coupling. The error bar is the standard deviation. **f**  $\delta_{\text{pb}}$  map corresponding to the dashed box in **(a)**. The insets in **(f)** depict the correspondence between colors and polar directions. The scale bars in **(c)** and **(f)** indicate 2 nm.

despite local fluctuations (Supplementary Fig. 11). Combining the analysis of planar and cross-sectional TEM samples, we speculate that the polarization configuration at the core of the dislocation corresponds to an antihedgehog structure, as illustrated in the three-dimensional schematic in Fig. 3f. Notably, the polar topological structure exhibits adaptability to slight irregular spacing of the dislocation array (Fig. 1e), and can adapt to these local perturbations without losing its fundamental order (Supplementary Fig. 12).

#### Phase-field simulations and theoretical rationalization

To elucidate the specific role of dislocations on the formation of the polar antihedgehog observed experimentally, systematic phase-field simulations were performed (details provided in the Methods section). As shown in Fig. 4a, the topological domain structure exhibits a checkerboard-like pattern composed of divergent (orange circles) and convergent (blue circles) polarization centers. Notably, the convergent

centers are precisely aligned with the dislocation cores (Fig. 4b and Supplementary Fig. 13), underscoring the essential role of dislocations in shaping the observed ordered structure. To further elucidate the polarization characteristics within the ordered arrays, the local polarization distribution in the highlighted region I in Fig. 4a was extracted and presented in Figs. 4c–4h. As shown in Figs. 4c–4e, the analysis identifies two distinct polarization behaviors: in the upper region, the polarization converges downward toward the dislocation, while in the lower part, the polarization converges upward toward the dislocation. Near the dislocation core, the region of upward-oriented polarization decreases from approximately 3 nm to about 1 nm along the  $[001]$  direction, with upward components concentrated only near the interface (Figs. 4d and 4e). Away from the interface, the polarization predominantly remains downward-oriented. Planar projections across different thicknesses in Figs. 4f–4h reveal a distinct trend of polarization convergence. As the polarization converges at the dislocation

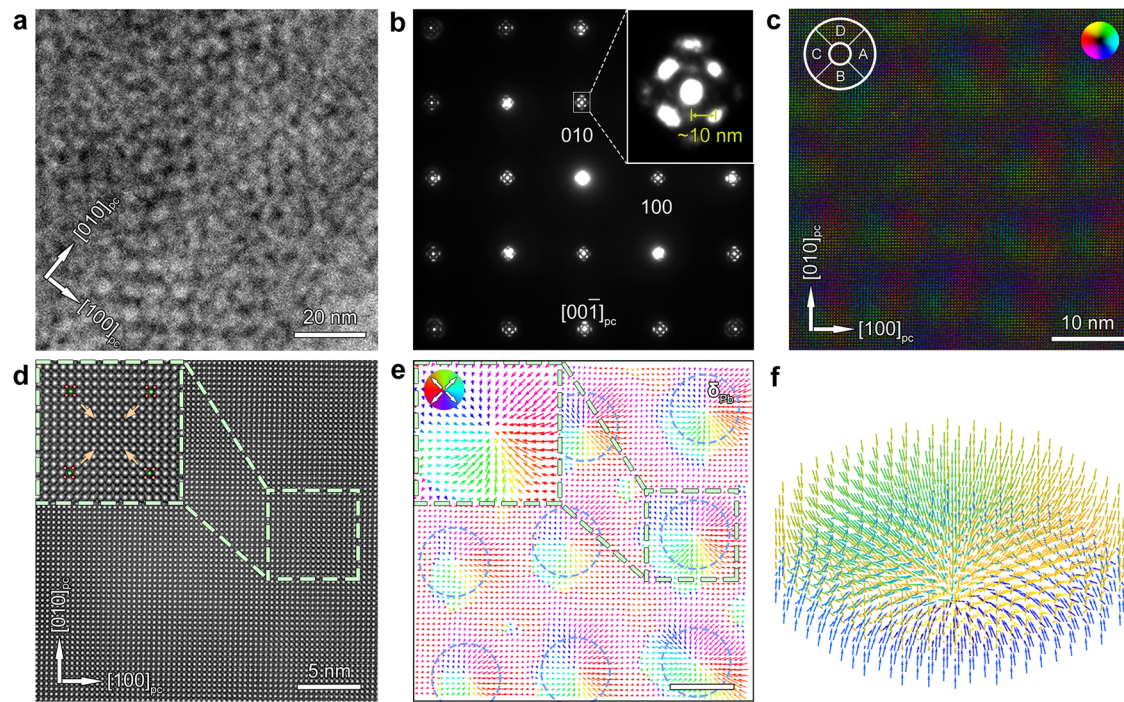


**Fig. 3 | Antihedgehogs in the planar-view TEM sample of PZO thin film.** **a** TEM topography of the PZO film displaying the ordered distribution of dot-like contrast. **b** SAED pattern of the PZO film along the [001] axis. **c** High-resolution electric vector color map of the ordered polar structures. The [100] and [010] directions of the PZO unit cells are aligned with the A-C and B-D segments of the detectors, respectively. **d** Atomic-resolved HAADF-STEM image of the planar-view TEM

sample. The light green dashed box shows the  $\text{Pb}^{2+}$  displacement direction for a convergence center. **e**  $\delta_{\text{Pb}}$  map corresponding to the PZO film in **(d)**. The insets depict the correspondence between colors and polar directions. **f** Schematic illustration of the three-dimensional center-convergent domains at the core of the dislocation. The scale bar in **(e)** indicates 5 nm.

cores in the upper region, a divergent polarization pattern emerges in the region enclosed by four adjacent dislocations, as highlighted as the region II in Fig. 4a and shown in Supplementary Fig. 14.

These configurations are reminiscent of the hedgehog and antihedgehog domains, with the former possessing a positive topological charge (Fig. 4i) and the latter a negative one (Fig. 4j). The topological charge of the region can be calculated using the formula<sup>7,38</sup>,  $Q = \frac{1}{8\pi} \int dA_i \varepsilon_{ijk} \hat{\mathbf{p}}(\mathbf{r}) \cdot [\partial_j \hat{\mathbf{p}}(\mathbf{r}) \times \partial_k \hat{\mathbf{p}}(\mathbf{r})]$ , where  $\hat{\mathbf{p}}$  is the normalized polarization vector,  $A_i$  is the surface enclosing the volume containing the topological region, and  $\varepsilon_{ijk}$  is the Levi-Civita symbol. The calculated topological charge is -1 for the polarization convergence unit in region I and -1 for the polarization divergence unit in region II, corresponding to two distinct types of topological configurations. The first represents a convergent-type antihedgehog structure, characterized by the inward orientation of polarization vectors toward a central singularity. In contrast, the second configuration exhibits a polarization field that converges vertically toward the core, forming a head-to-tail alignment along the out-of-plane direction, while diverging laterally within the plane toward the opposite edges. This combination of vertical convergence and in-plane divergence gives rise to a composite topological texture, closely resembling the divergent-divergent-convergent-type Bloch point reported in our previous work<sup>7</sup>. The combination of polarizations converging at dislocation cores and diverging between dislocations defines a lattice characterized by checkerboard-like antihedgehog (Fig. 4k).

The formation of the novel polar antihedgehog structure is attributed to the interplay between the electrostrictive effect and the flexoelectric field induced by the dislocation network. First, the periodic strain field of the dislocation network (Fig. 4b and Supplementary Fig. 13) significantly reconstructs the local polarization distribution by altering the local lattice environment. In addition, the strain gradient

associated with the dislocation field cannot be neglected. As illustrated in Figs. 5a–5d and Supplementary Fig. 15, strong strain gradients emerge near the dislocation cores, particularly along the out-of-plane direction. The gradients of the normal strains ( $\varepsilon_{xx}$ ,  $\varepsilon_{zz}$ ) and the shear strain ( $\varepsilon_{xz}$ ) along [001] are much larger than those in-plane, with the maximum  $\varepsilon_{xx,z}$  reaching  $4.8 \times 10^8 \text{ m}^{-1}$ . The resultant flexoelectric field shown in Figs. 5e–5j is highly localized at the interface. The calculated in-plane flexoelectric field  $E_x^{\text{flexo}}$  and  $E_y^{\text{flexo}}$  (Fig. 5i and Supplementary Fig. 16) exhibits opposite directions on either side of the dislocation line. Specifically,  $E_x^{\text{flexo}}$  is positive on the left of the dislocation line and negative on the right with an absolute peak magnitude of 6.8 MV/cm, which drives the polarization between adjacent dislocation cores near the interface to converge toward the dislocation core. In addition, the pronounced out-of-plane strain gradient amplifies  $E_z^{\text{flexo}}$ , which reaches a positive value of 34 MV/cm near the interface and drives the polarization to reverse from downward to upward. This strong, localized flexoelectric field drives polarization in the interface region to flip upward and converge toward the dislocation core. Hence, the synergistic interaction between the electrostrictive effect and the highly localized flexoelectric field is essential for stabilizing the polar antihedgehog structure. In contrast, as illustrated in Supplementary Fig. 17, in the absence of the flexoelectric field, the out-of-plane polarizations show a convergence pattern. For the in-plane polarizations, those in the upper region exhibit pronounced convergence toward the dislocation core, while those in the lower region show a divergent pattern, different from the experimental observation.

### Chemical analysis of dislocation cores and emergent properties

To assess potential chemical changes induced by dislocation strain fields<sup>39</sup>, we performed atomic-resolution electron energy loss spectroscopy (EELS) near the dislocation cores. Atomic-scale EELS

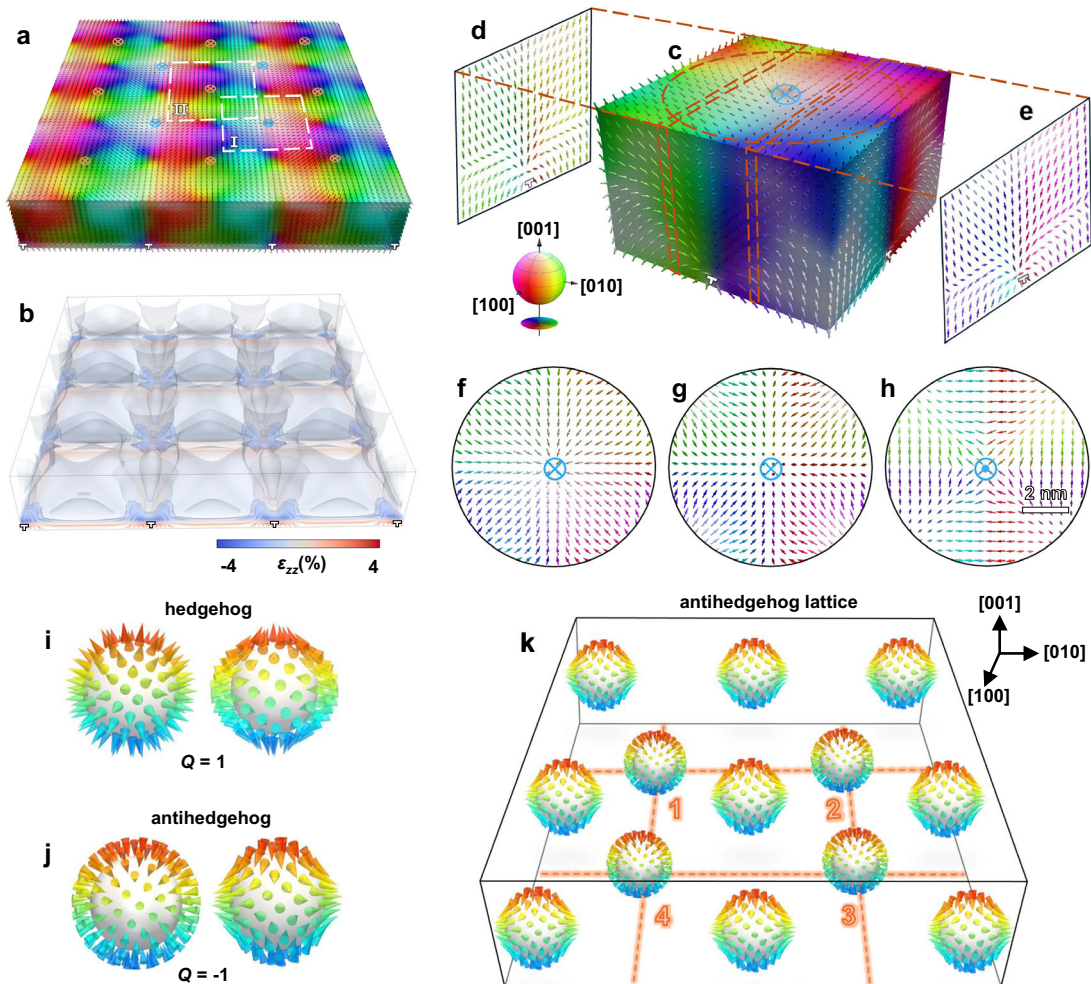


**Fig. 4 | Polarization characteristics of the ordered topological domain obtained from phase-field simulations.** **a** Three-dimensional polarization arrangement showing a convergence unit (region I, blue circles) and a divergence unit (region II, orange circles). Crosses and dots indicate polarization pointing into and out of the page, respectively. **b** Isosurface representation of the strain component  $\varepsilon_{zz}$ . **c–e** Detailed visualization of the polarization structure within the region I (blue circles) of **(a)**. **(d)** and **(e)** show cross-sectional views of the marked areas in **(c)**.

**f–h** Planar polarization distributions across different thicknesses of **(c)**: **(f)** the top layer, **(g)** the middle layer, and **(h)** the bottom layer. The divergent configuration (region II, orange circles) is shown in Supplementary Fig. 14. **i, j** Integer hedgehog and antihedgehog domains. **k** Schematic diagram of a lattice characterized by checkerboard-like antihedgehogs. The brown dashed lines denote the dislocations. The number “1–4” marked the position of the type-2 antihedgehogs.

elemental mapping (Figs. 6a–6h) shows no significant chemical inhomogeneity. This reveals the elemental distribution above the interface are not affected by the dislocations, showing no clear sign of chemical aggregation or deficiency in the PZO films. These combined results suggest that the observed polar topological structures originate primarily from strain gradients and flexoelectric effects, rather than from chemical inhomogeneity.

Recent work has established that local negative capacitance can emerge within a range of ferroelectric topological textures, including skyrmions, and Bloch points<sup>7,40</sup>. Here, we resolve the spatial arrangement of the antihedgehog lattice in the PZO film (Fig. 6i). Remarkably, both the polarization-converging cores (orange arrows) and the polarization-diverging cores (blue arrows) exhibit regions of negative dielectric permittivity, as captured by the  $\varepsilon_{zz} = -500$  isosurface. The manifestation of negative capacitance at these distinct topological centers emphasizes the functional role of the antihedgehog lattice in shaping the local electrostatic landscape and reveals a direct link between polar topology and dielectric response.

Moreover, the influence of the dislocation strain field is spatially limited. As thickness increases, the strain gradient relaxes with

distance from the interface (Supplementary Note 2). Both experimental and computational results indicate that the polarization rotation is primarily confined to a thickness of approximately 5 nm (Supplementary Figs. 18 and 19). Beyond this range, the effect of the dislocation strain field diminishes significantly, leading to a minimal influence on the polarization, with the in-plane component becoming effectively absent near the surface. To quantitatively reveal the piezoresponse behaviors of the above topological structure, local butterfly loops of the PZO films with different thicknesses are measured using an atomic force microscope equipped with an interferometric displacement sensor (IDS). Representative piezoresponse amplitude loops for 5 nm, 7 nm, and 9 nm PZO films are shown in Fig. 6j, with the corresponding effective  $d_{33}$  peak values summarized in Fig. 6k. The 5 nm PZO film hosting the antihedgehog lattice exhibits higher  $d_{33}$  value of -10.6 pm/V, exceeding those of the 7 nm (-5.8 pm/V) and 9 nm (-8.4 pm/V) films. This trend is different from the strong thickness dependence typically observed in ferroelectric  $d_{33}$  for systems such as BaTiO<sub>3</sub><sup>41</sup>, and highlights the role of the ordered topological structure in enhancing the electromechanical response. The magnitude of this response is comparable to that reported for 8 nm-thick BiFeO<sub>3</sub> films

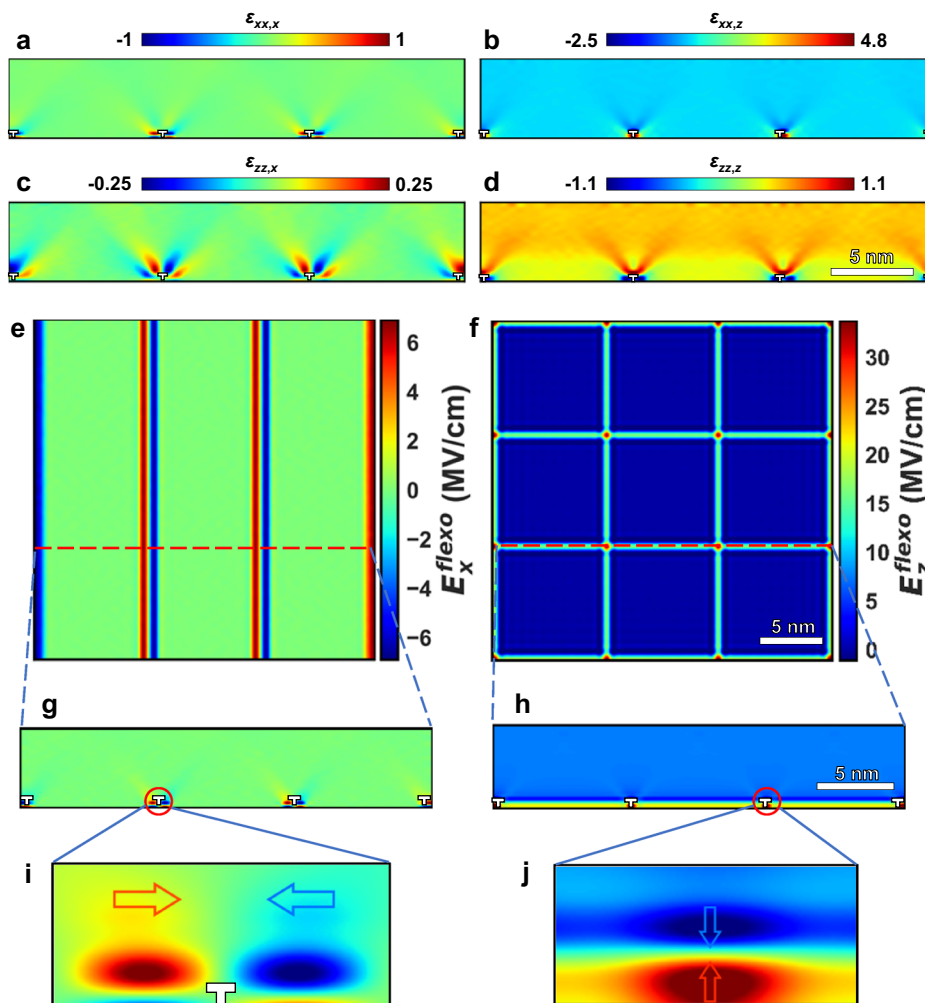


**Fig. 5 | Coupled strain-gradient and flexoelectric fields in the formation of the topological lattice.** **a–d** Strain gradient distributions on the (100) plane with  $f_{11} = f_{12} = 1\text{V}$  and  $f_{44} = 0.5\text{V}$ . Additional results are shown in Supplementary Fig. 15. **e, f** In-plane  $E_x^{\text{flexo}}$  and  $E_z^{\text{flexo}}$  components in the plane containing the dislocation,

showing flexoelectric field distributions induced by strain gradients via the flexoelectric effect. **g, h** Cross-sectional distributions along the red dashed lines in (**e–f**). **i, j** Enlarged local electric-field components with arrows indicating field directions. The  $E_y^{\text{flexo}}$  distribution is shown in Supplementary Fig. 16.

containing polar skyrmion superlattices ( $d_{33} \sim 9.0 \text{ pm/V}$ )<sup>42</sup>, underscoring the potential of topology-engineered phases in functional oxide devices.

To further demonstrate the field-tunable nature of the dislocation-stabilized antihedgehog lattice, we performed phase-field simulations under an applied out-of-plane electric field. The results, presented in Supplementary Fig. 20, show that the local polarization within the antihedgehog domains undergoes a reversible switching process in response to the external field. Upon application of a sufficiently strong bias of 2.0 MV/cm, the polarization at both the converging and diverging topological centers is reoriented, leading to a controlled reconfiguration of the lattice. Notably, once the electric field is removed, the system spontaneously relaxes back to its initial topological state, highlighting the recoverable and dynamically reconfigurable character of the antihedgehog lattice.

## Discussion

The exploration of polar topological structures has predominantly focused on ferroelectric thin films, with notable examples including  $\text{PbTiO}_3/\text{SrTiO}_3$  superlattices<sup>2–5</sup>, ultrathin  $\text{PbTiO}_3$  films<sup>6</sup>, and  $\text{BiFeO}_3$  systems<sup>43,44</sup>. More recently, Govinden et al. reported in  $\text{BiFeO}_3/\text{SrTiO}_3$  superlattices that center-convergent/divergent topological defects can be classed as bimerons, and that the coexistence of such structures

can lead to noninteger topological charges<sup>45</sup>. In this study, we reveal unexpectedly strong couplings between polar and structural topologies and realize for the first time an ordered polar antihedgehog lattice in antiferroelectrics, marking a transformative step in the search for exotic topological domains in antiferroelectrics. This achievement is enabled by the innovative use of high-density dislocation arrays as a modulation strategy, which not only drives the emergence of the ordered polar topology but also provides a powerful platform for investigating the intricate interplay among spin, charge, orbital, and lattice degrees of freedom in strongly correlated systems. Beyond the demonstrated antiferroelectric system, this methodology holds great potential for harnessing lattice strains and one-dimensional topological structures arising from lattice mismatches, unlocking pathways to exotic structural modulations and polar topologies across a wide range of functional materials.

Since dislocations are the most common one-dimensional topological structure in crystals, our results then have broad illuminations for future studies toward the interactions of interfacial dislocations and other potential physical topologies.

In summary, we have unveiled a polar antihedgehog lattice introduced by high-density dislocation arrays in antiferroelectric materials using transmission electron microscopy imaging and phase-field simulations. This study reveals that the interface dislocations,

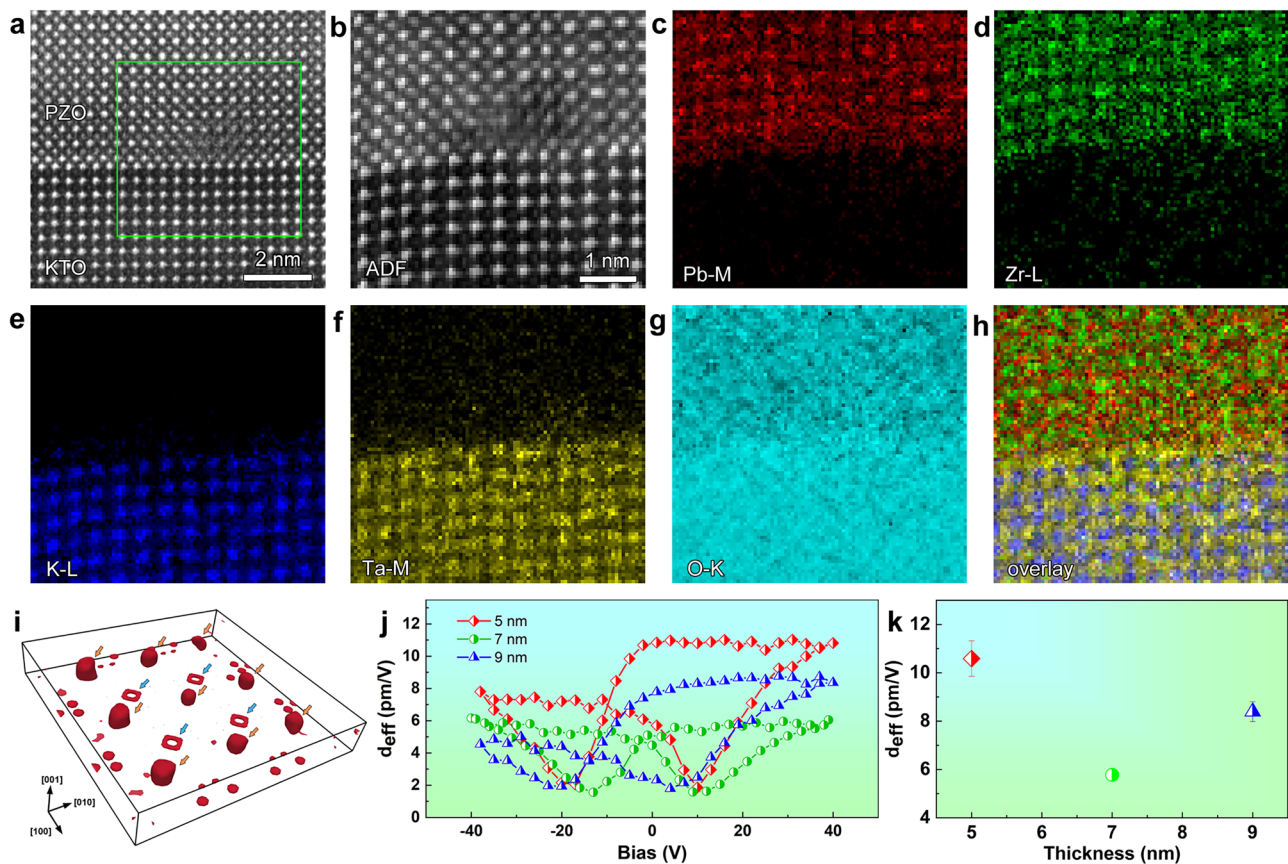


**Fig. 6 | Element distribution around interface dislocations and its emergent properties.** **a** Atomic-resolved HAADF-STEM image of PZO/KTO film. The green box outlines the location of the EELS maps. **b** Corresponding to the EELS spectrum acquisition region within the green box in (a). **c–g** EELS atomic maps of Pb-M edge, Zr-L edge, K-L edge, Ta-M edge and O-K edge. **h** A RGB composite map of the Pb-M edge, Zr-L edge, K-L edge and Ta-M edge. **i** Local negative capacitance around

antihedgehog domains revealed by phase-field simulations. The isosurface of  $\varepsilon_{zz} = -500$  is shown in red. Two different types of antihedgehog domains, indicated by orange and blue arrows, correspond to polarization convergence centers and divergence centers, respectively. **j** Representative piezoresponse amplitude loops of PZO films with varying thicknesses. **k** Effective  $d_{33}$  of PZO films with different thicknesses. The error bar is the standard deviation.

typical one-dimensional topological structure in crystals, can be harnessed as an effective factor for manipulating polar structures, underscoring the potential of utilizing one-dimensional topological structures in epitaxial systems to design and realize novel polar topologies. Furthermore, the robust interplay between polar and structural topologies in antiferroelectrics can provide unprecedented opportunities to exploit their distinct properties. The demonstrated concept of dislocation-mediated polar topology control opens broader opportunities for designing correlated polar textures in quantum materials. We anticipate that this cross-scale coupling will establish a new paradigm for the development of high-performance electronic devices through the interplay of polar and structural topologies.

## Methods

### Film deposition details

A series of epitaxial  $\text{PbZrO}_3$  (PZO) ultrathin films were grown on single-crystal  $\text{KTaO}_3$  (001) substrates by PLD, using a Coherent ComPexPRO 201KrF excimer laser ( $\lambda = 248$  nm). The  $\text{KTaO}_3$  (001) substrates used here are commercial substrates without extra chemical or heat treatment. Before film deposition, the substrate was heated up to  $800^\circ\text{C}$  with a heating rate of  $25^\circ\text{C}/\text{min}$  stayed for 5 minutes to clean the substrate surface and the laser was focused on a ceramic PZO target for 10 minutes pre-sputtering to clean the target surface. Then cooled down to  $700^\circ\text{C}$  with a cooling rate of  $15^\circ\text{C}/\text{min}$  to grow the PZO films. Throughout the deposition process, an oxygen pressure of 6.6 Pa, a

laser repetition rate of 4 Hz, and a laser energy of 200 mJ were used. After deposition, these samples were stabilized at  $700^\circ\text{C}$  for 5 minutes and then cooled down to room temperature at a cooling rate of  $5^\circ\text{C}/\text{min}$  in an oxygen pressure of  $2.6 \times 10^4$  Pa.

### Structural analysis

Crystal structure study was performed by X-ray  $\theta$ - $2\theta$  scans and reciprocal space mappings (RSMs) using a high-resolution X-ray diffractometer (Bruker D8 Discover X-ray diffractometer,  $\lambda = 1.5406$  Å).

### TEM, STEM and determining the positions of atom columns

Cross-sectional samples for TEM and STEM imaging were prepared by slicing, gluing, grinding, dimpling, and finally ion milling by using Precision Ion Polishing System 691 of Gatan company. Before ion milling, the samples were dimpled down to  $10\ \mu\text{m}$  by Gatan 657 Dimple Grinder. During the ion milling, a voltage of 4.5 kV and an incident angle of  $7^\circ$  were used at first, and then the voltage and incident angle were gradually reduced to 4.0 kV and  $5^\circ$ , respectively. The final ion milling voltage was 0.1 kV for 5 min to reduce the amorphous layer produced in the milling process. Unlike the cross-sectional samples, the plane-view sample was milled only from the substrate side to protect the film from damage.

Dark-field images and selected area electron diffraction (SAED) patterns were acquired by JEOL F200 high-resolution TEM. High-angle annular dark-field (HAADF) STEM images were acquired using ThermoFisher Spectra 300 microscope with a high-brightness field-

emission gun, double aberration (Cs) correctors from CEOS operating at 300 kV. The beam convergence angle is 25 mrad, and the collection angle ranges from 36 mrad to 200 mrad. Each of the atomic-scale HAADF-STEM images was acquired by adding up 20 original images, recorded from the same area. Image acquisition and processing were performed using the Velox software (FEI). Acquiring images in this way can reduce the influence of sample drift and scanning noises. (i)DPC-STEM imaging was performed with a convergence angle of 25 mrad and a panther detector. The thickness ranges of planar-view and cross-sectional samples from -20 nm to 30 nm as measured by electron energy loss spectroscopy (EELS). The EELS elemental mapping data were acquired using K3 camera in Gatan Digital Micrograph software, with a dispersion of 0.9 eV/Ch. The large-scale strain fields were extracted by using geometry phase analysis (GPA)<sup>46</sup>, carried out by Gatan Digital Micrograph software.

By using a two-dimensional Gaussian peaks fitting<sup>47</sup> in Matlab software, the atom positions can be accurately determined<sup>48</sup>, thus making it possible to acquire information of the lattice spacing, lattice rotation, and ionic displacement. The lattice rotation is defined as the deviation angle of each lattice unit relative to the ideal crystal axes (horizontal x and vertical y directions), with clockwise and counterclockwise rotations assigned as negative and positive, respectively. The resulting parameters,  $R_x$  and  $R_y$ , not only provide a quantitative measure of lattice rotation along each axis but, more importantly, collectively reflect the local lattice distortions induced by dislocation strain fields. In perovskite-structured PZO materials, the polarization primarily originates from the displacement of  $Pb^{2+}$  cations. Based on this, the present study characterizes the displacement vector of the  $Pb^{2+}$  cations by calculating the displacement of Pb atom column relative to the geometric center of the surrounding four Zr atomic columns, thereby approximating the polarization direction equivalently.

### Phase-field simulation

In the three-dimensional phase-field modeling of the PZO system, the spontaneous polarization components  $P_i$  ( $i=1, 2, 3$ ) are selected as the order parameters. The corresponding temporal evolution follows the time-dependent Ginzburg-Landau (TDGL) equation<sup>49</sup>:

$$\frac{\partial P_i(\mathbf{r}, t)}{\partial t} = -L_i \frac{\delta F}{\delta P_i(\mathbf{r}, t)}, (i=1, 2, 3) \quad (1)$$

where  $L_i$  represents the kinetic coefficient associated with the domain wall mobility and  $\delta F/\delta P_i(\mathbf{r}, t)$  signifies the driving force governing the spatial and temporal behavior of  $P_i(\mathbf{r}, t)$ . The total free energy  $F$  accounts for contributions from bulk, gradient, elastic, electrostatic, and flexoelectric energies, formulated as:

$$F = \int \int \int (f_{bulk} + f_{grad} + f_{elas} + f_{elec} + f_{flexo}) dV \quad (2)$$

where  $V$  is the volume of the film.

The expression of bulk free energy density is as follows:

$$f_{bulk} = \alpha_1 (P_1^2 + P_2^2 + P_3^2) + \alpha_{11} (P_1^4 + P_2^4 + P_3^4) + \alpha_{12} (P_1^2 P_2^2 + P_2^2 P_3^2 + P_1^2 P_3^2) + \alpha_{111} (P_1^6 + P_2^6 + P_3^6) + \alpha_{112} [P_1^4 (P_2^2 + P_3^2) + P_2^4 (P_1^2 + P_3^2) + P_3^4 (P_1^2 + P_2^2)] + \alpha_{123} P_1^2 P_2^2 P_3^2 \quad (3)$$

where  $\alpha_i$ ,  $\alpha_{ij}$ , and  $\alpha_{ijk}$  are local potential coefficients representing the stiffness with respect to polarization changes.

The gradient energy density can be expressed as<sup>50,51</sup>:

$$f_{grad} = \sum_i \left\{ \lambda_0 \left[ \left( \frac{\partial P_i}{\partial x} \right)^2 + \left( \frac{\partial P_i}{\partial y} \right)^2 + \left( \frac{\partial P_i}{\partial z} \right)^2 \right] + g_0 \left[ \left( \frac{\partial^2 P_i}{\partial x^2} \right)^2 + \left( \frac{\partial^2 P_i}{\partial y^2} \right)^2 + \left( \frac{\partial^2 P_i}{\partial z^2} \right)^2 \right] \right\} \quad (4)$$

Here,  $\lambda_0$  is a negative constant which stabilizes the AFE phase by accounting for the coupling between polarization and oxygen octahedral tilts. In contrast,  $g_0$  is a positive constant representing the next-nearest-neighbor interaction among polarizations, driving the phase transition from AFE to FE. In this work, the renormalized values of  $\lambda_0 = -0.1$  and  $g_0 = 0.3$  are adopted to simulate the FE phase observed in the ultrathin PZO film.

The elastic energy density can be written as:

$$f_{elas} = \frac{1}{2} C_{ijkl} (\varepsilon_{ij} - \varepsilon_{ij}^0) (\varepsilon_{kl} - \varepsilon_{kl}^0) \quad (5)$$

in which  $\varepsilon_{ij}$  is the total strain and  $\varepsilon_{ij}^0$  represents the eigenstrain. The difference  $\varepsilon_{ij} - \varepsilon_{ij}^0$  corresponds to the elastic strain. In this work, the eigenstrain  $\varepsilon_{ij}^0$  is decomposed into two components: the spontaneous polarization-induced strain  $\varepsilon_{ij}^{0P}$  and the dislocation-induced strain  $\varepsilon_{ij}^{0D}$ :  $\varepsilon_{ij}^0 = \varepsilon_{ij}^{0P} + \varepsilon_{ij}^{0D}$ . The spontaneous strain,  $\varepsilon_{ij}^{0P} = Q_{ijkl} P_k P_l$ , is related to be the polarization through electrostrictive coefficients  $Q_{ijkl}$ . For a dislocation loop located on a slip plane  $\mathbf{s}$  with a Burgers vector  $\mathbf{b} = (b_1, b_2, b_3)$ , the induced strain is given by  $\varepsilon_{ij}^{0D} = \frac{1}{2d_0} [(b_i n_j + b_j n_i)] \delta(x - x^D)$  where  $\mathbf{n} = (n_1, n_2, n_3)$  is unit vector normal to the slip plane,  $d_0$  is the interplanar distance of the slip plane,  $\delta(x - x^D)$  is the Dirac delta function, and  $x^D$  is a point inside the dislocation loop. To model the experimentally observed dislocation networks, the simulation incorporates an ordered dislocation array, which consists of dislocation lines with Burgers vectors  $\mathbf{b} = a[010]$  along the  $[010]$  direction and  $\mathbf{b} = a[\bar{1}00]$  along the  $[100]$  direction. The spacing between adjacent dislocation lines is set as approximately 9 nm, consistent with experimentally measured dislocation spacings.

The electrostatic energy density can be expressed as:

$$f_{elec} = -\frac{1}{2} \varepsilon_0 \varepsilon_b E_i^2 - E_i P_i \quad (6)$$

where  $E_i$  is the electric field component,  $\varepsilon_0$  is the permittivity of vacuum and  $\varepsilon_b$  is the background dielectric constant.

The last term is the flexoelectric energy density:

$$f_{flexo} = \frac{f_{ijkl}}{2} \left( \varepsilon_{ij} \frac{\partial P_k}{\partial x_l} - P_k \frac{\varepsilon_{ij}}{\partial x_l} \right) \quad (7)$$

where  $f_{ijkl}$  represents the flexocoupling coefficient tensor<sup>52,53</sup>. In Voigt notation, the components are simplified as  $f_{11} = f_{1111}$ ,  $f_{12} = f_{1122}$ , and  $f_{44} = 2f_{1212}$ . Given the uncertainties in the exact magnitude of  $f_{ijkl}$ , we use  $f_{11} = f_{12} = 1V$  and assume  $f_{44} = 0.5V$  for simplicity based on the reasonable estimation from previous literatures<sup>54,55</sup>. The driving force from the flexoelectric effect yields the flexoelectric field  $E_k^{flexo}$ :

$$\frac{\delta f_{flexo}}{\delta P_k} = \frac{\partial f_{flexo}}{\partial P_k} - \frac{\partial}{\partial x_l} \left( \frac{\partial f_{flexo}}{\partial P_k / \partial x_l} \right) = -f_{ijkl} \frac{\partial \varepsilon_{ij}}{\partial x_l} = -E_k^{flexo} \quad (8)$$

Mechanical stress and electric field equilibrium is assumed to arrive much faster than the evolution of domain structures. Thus, we

solve the mechanical equilibrium equations and Maxwell equation:

$$\begin{aligned}\sigma_{ij,j} &= 0 \\ D_{i,i} &= 0\end{aligned}\quad (9)$$

to obtain the corresponding driving forces for each polarization configuration.

The three-dimensional computational domain is discretized into a  $64\Delta x \times 64\Delta y \times 24\Delta z$  mesh. The grid spaces are  $\Delta x = \Delta y = a_c$  and  $\Delta z = a_c/2$ , where  $a_c = \frac{a_0}{\sqrt{2}} = 0.416$  nm, setting up a 5 nm-thick PZO film. Beneath the PZO film, a substrate layer of 20 grids thickness is included to emulate a deformable substrate. Above the PZO film, a vacuum layer with a thickness of 12 grid points is incorporated. The material parameters of PZO are sourced from prior literature<sup>51</sup> and summarized in Supplementary Table 1. Periodic boundary condition is applied along the in-plane directions. The mechanical boundary conditions are defined as a traction-free top surface for the PZO film and a fully constrained bottom surface for the deformable substrate. Additionally, short-circuit electrical boundary conditions are imposed on the top and bottom surfaces of the PZO layer. The initial domain configuration is set as a single-domain state, with the polarization oriented entirely downward. Considering that dislocations relieve most of the substrate-induced strain, only a -1% compressive strain is applied to stabilize the out-of-plane domain configuration.

We evaluate the local out-of-plane dielectric constant  $\varepsilon_{zz}$ , defined as the functional derivative of the electric displacement  $D_z$  with respect to the total electric field  $E_z$ :  $\varepsilon_{zz} = \partial D_z / \partial E_z$ . The electric displacement is given by  $D_z = \varepsilon_0 \varepsilon_b E_z + P_z$ , where  $\varepsilon_0$  is the vacuum permittivity,  $\varepsilon_b$  is the background dielectric constant, and  $P_z$  is the local polarization. To compute  $\varepsilon_{zz}$ , a small probing electric field of 400 kV/cm is applied along the out-of-plane direction. The resulting variations in  $D_z$  and  $E_z$  are evaluated at each grid point, from which the local dielectric response is obtained.

## Data availability

All data that support the main findings are available in the main text and the Supplementary Information or from the corresponding authors upon request. Source data for Figs. 1–3 and 6 are provided with the paper. Source data are provided with this paper.

## Code availability

The computer code that supports the findings of this study is available from the corresponding authors upon reasonable request.

## References

- Wen, X.-G. *Colloquium: Zoo of quantum-topological phases of matter*. *Rev. Mod. Phys.* **89**, 041004 (2017).
- Tang, Y. L. et al. Observation of a periodic array of flux-closure quadrants in strained ferroelectric PbTiO<sub>3</sub> films. *Science* **348**, 547–551 (2015).
- Yadav, A. K. et al. Observation of polar vortices in oxide superlattices. *Nature* **530**, 198–201 (2016).
- Das, S. et al. Observation of room-temperature polar skyrmions. *Nature* **568**, 368–372 (2019).
- Gong, F.-H. et al. Atomic mapping of periodic dipole waves in ferroelectric oxide. *Sci. Adv.* **7**, eabg5503 (2021).
- Wang, Y. J. et al. Polar meron lattice in strained oxide ferroelectrics. *Nat. Mater.* **19**, 881–886 (2020).
- Wang, Y.-J. et al. Polar Bloch points in strained ferroelectric films. *Nat. Commun.* **15**, 3949 (2024).
- Liu, Z. et al. Antiferroelectrics for energy storage applications: A review. *Adv. Mater. Technol.* **3**, 1800111 (2018).
- Yang, B. et al. Enhanced energy storage in antiferroelectrics via antipolar frustration. *Nature* **637**, 1104–1110 (2025).
- Zhuo, F. et al. Large field-induced strain, giant strain memory effect, and high thermal stability energy storage in (Pb,La)(Zr,Sn,Ti)O<sub>3</sub> antiferroelectric single crystal. *Acta Mater.* **148**, 28–37 (2018).
- Mischenko, A. S., Zhang, Q., Scott, J. F., Whatmore, R. W. & Mathur, N. D. Giant electrocaloric effect in thin-film PbZr<sub>0.95</sub>Ti<sub>0.05</sub>O<sub>3</sub>. *Science* **311**, 1270–1271 (2006).
- Geng, W. et al. Giant negative electrocaloric effect in antiferroelectric La-doped Pb(ZrTi)O<sub>3</sub> thin films near room temperature. *Adv. Mater.* **27**, 3165–3169 (2015).
- Liu, C. et al. Low voltage-driven high-performance thermal switching in antiferroelectric PbZrO<sub>3</sub> thin films. *Science* **382**, 1265–1269 (2023).
- Yao, Y. et al. Ferrielectricity in the archetypal antiferroelectric, PbZrO<sub>3</sub>. *Adv. Mater.* **35**, 2206541 (2023).
- Pan, H. et al. Clamping enables enhanced electromechanical responses in antiferroelectric thin films. *Nat. Mater.* **23**, 944–950 (2024).
- Fu, Z. Q. et al. Unveiling the ferrielectric nature of PbZrO<sub>3</sub>-based antiferroelectric materials. *Nat. Commun.* **11**, 3809 (2020).
- Li, Z. et al. Discovery of electric devil's staircase in perovskite antiferroelectric. *Sci. Adv.* **8**, eabl9088 (2022).
- Jiang, R.-J. et al. Atomic insight into the successive antiferroelectric-ferroelectric phase transition in antiferroelectric oxides. *Nano Lett.* **23**, 1522–1529 (2023).
- Si, Y. et al. Antiferroelectric oxide thin-films: Fundamentals, properties, and applications. *Prog. Mater. Sci.* **142**, 101231 (2024).
- Jiang, R.-J. et al. A roadmap for ferroelectric–antiferroelectric phase transition. *Nano Lett.* **24**, 11714–11721 (2024).
- Corker, D. L., Glazer, A. M., Dec, J., Roleder, K. & Whatmore, R. W. A re-investigation of the crystal structure of the perovskite PbZrO<sub>3</sub> by X-ray and neutron diffraction. *Acta Crystallogr., Sect. B: Struct. Sci.* **53**, 135–142 (1997).
- Tang, Y. L., Zhu, Y. L., Liu, Y., Wang, Y. J. & Ma, X. L. Giant linear strain gradient with extremely low elastic energy in a perovskite nanostructure array. *Nat. Commun.* **8**, 15994 (2017).
- Gao, P. et al. Atomic-scale measurement of flexoelectric polarization at SrTiO<sub>3</sub> dislocations. *Phys. Rev. Lett.* **120**, 267601 (2018).
- Geng, W. et al. Atomic-scale tunable flexoelectric couplings in oxide multiferroics. *Nano Lett.* **21**, 9601–9608 (2021).
- Jia, C. L. et al. Effect of a single dislocation in a heterostructure layer on the local polarization of a ferroelectric layer. *Phys. Rev. Lett.* **102**, 117601 (2009).
- Xu, Y. B. et al. Misfit strain relaxation of ferroelectric PbTiO<sub>3</sub>/LaAlO<sub>3</sub> (111) thin film system. *Sci. Rep.* **6**, 35172 (2016).
- Feng, Y. P. et al. Strain coupling of ferroelastic domains and misfit dislocations in [101]-oriented ferroelectric PbTiO<sub>3</sub> films. *Rsc Adv.* **12**, 20423–20431 (2022).
- Li, X. et al. Dislocation-tuned ferroelectricity and ferromagnetism of the BiFeO<sub>3</sub>/SrRuO<sub>3</sub> interface. *Proc. Natl. Acad. Sci.* **120**, e2213650120 (2023).
- Cheng, X. X., Wang, B. & Chen, L. Q. Polarization near dislocation cores in SrTiO<sub>3</sub> single crystals: The role of flexoelectricity. *Appl. Phys. Lett.* **124**, 132905 (2024).
- Li, Z. et al. High-density array of ferroelectric nanodots with robust and reversibly switchable topological domain states. *Sci. Adv.* **3**, e1700919 (2017).
- Ma, J. et al. Controllable conductive readout in self-assembled, topologically confined ferroelectric domain walls. *Nat. Nanotechnol.* **13**, 947–952 (2018).
- Yang, W. D. et al. Quasi-one-dimensional metallic conduction channels in exotic ferroelectric topological defects. *Nat. Commun.* **12**, 1306 (2021).
- Han, M.-J. et al. Shape and surface charge modulation of topological domains in oxide multiferroics. *J. Phys. Chem. C.* **123**, 2557–2564 (2019).

34. Mermin, N. D. Topological theory of defects in ordered media. *Rev. Mod. Phys.* **51**, 591–648 (1979).
  35. Chen, S. et al. Recent progress on topological structures in ferroic thin films and heterostructures. *Adv. Mater.* **33**, 2000857 (2021).
  36. Wang, Y. J., Tang, Y. L., Zhu, Y. L. & Ma, X. L. Entangled polarizations in ferroelectrics: A focused review of polar topologies. *Acta Mater.* **243**, 118485 (2023).
  37. Shibata, N. et al. Differential phase-contrast microscopy at atomic resolution. *Nat. Phys.* **8**, 611–615 (2012).
  38. Im, M.-Y. et al. Dynamics of the Bloch point in an asymmetric permalloy disk. *Nat. Commun.* **10**, 593 (2019).
  39. Arredondo, M. et al. Direct evidence for cation non-stoichiometry and Cottrell atmospheres around dislocation cores in functional oxide interfaces. *Adv. Mater.* **22**, 2430–2434 (2010).
  40. Das, S. et al. Local negative permittivity and topological phase transition in polar skyrmions. *Nat. Mater.* **20**, 194–201 (2021).
  41. Kelley, K. P. et al. Thickness and strain dependence of piezoelectric coefficient in BaTiO<sub>3</sub> thin films. *Phys. Rev. Mater.* **4**, 024407 (2020).
  42. Geng, W. R. et al. Dipolar wavevector interference induces a polar skyrmion lattice in strained BiFeO<sub>3</sub> films. *Nat. Nanotechnol.* **20**, 366–373 (2025).
  43. Geng, W. et al. Rhombohedral-orthorhombic ferroelectric morphotropic phase boundary associated with a polar vortex in BiFeO<sub>3</sub> films. *ACS Nano* **12**, 11098–11105 (2018).
  44. Vasudevan, R. K. et al. Exploring topological defects in epitaxial BiFeO<sub>3</sub> thin films. *ACS Nano* **5**, 879–887 (2011).
  45. Govinden, V. et al. Ferroelectric solitons crafted in epitaxial bismuth ferrite superlattices. *Nat. Commun.* **14**, 4178 (2023).
  46. Hÿtch, M. J., Snoeck, E. & Kilaas, R. Quantitative measurement of displacement and strain fields from HREM micrographs. *Ultra-microscopy* **74**, 131–146 (1998).
  47. Anthony, S. M. & Granick, S. Image analysis with rapid and accurate two-dimensional Gaussian fitting. *Langmuir* **25**, 8152–8160 (2009).
  48. Jia, C.-L. et al. Unit-cell scale mapping of ferroelectricity and tetragonality in epitaxial ultrathin ferroelectric films. *Nat. Mater.* **6**, 64–69 (2007).
  49. Li, Y. L., Hu, S. Y., Liu, Z. K. & Chen, L. Q. Effect of substrate constraint on the stability and evolution of ferroelectric domain structures in thin films. *Acta Mater.* **50**, 395–411 (2002).
  50. Xu, K., Shi, X., Dong, S., Wang, J. & Huang, H. Antiferroelectric phase diagram enhancing energy-storage performance by phase-field simulations. *ACS Appl. Mater. Interf.* **14**, 25770–25780 (2022).
  51. Liu, Z. & Xu, B.-X. Insight into perovskite antiferroelectric phases: Landau theory and phase field study. *Scr. Mater.* **186**, 136–141 (2020).
  52. Cao, Y., Morozovska, A. & Kalinin, S. V. Pressure-induced switching in ferroelectrics: Phase-field modeling, electrochemistry, flexoelectric effect, and bulk vacancy dynamics. *Phys. Rev. B* **96**, 184109 (2017).
  53. Eliseev, E. A., Morozovska, A. N., Glinchuk, M. D. & Blinc, R. Spontaneous flexoelectric/flexomagnetic effect in nanoferroics. *Phys. Rev. B* **79**, 165433 (2009).
  54. Liu, D. et al. Phase-field simulations of vortex chirality manipulation in ferroelectric thin films. *npj Quantum Mater.* **7**, 34 (2022).
  55. Park, S. M. et al. Selective control of multiple ferroelectric switching pathways using a trailing flexoelectric field. *Nat. Nanotechnol.* **13**, 366–370 (2018).
- (2024YFA1408000 (Y.-L.T.)), the Liaoning Revitalization Talents Program (XLYC2403183 (Y.-L.T.), XLYC2203020 (Y.-J.W.)), the Natural Science Foundation of Liaoning (2025010060-JH6/1011 (Y.-L.T.)), the Science and Technology Major Project of Liaoning province (2024JH1/11700033 (Y.-L.T.)), the IMR Innovation Fund (2024-ZD01 (Y.-L.T.)), Guangdong Provincial Quantum Science Strategic Initiative (GDZX2402001 (X.-L.M.)), GDZX2502004 (X.-L.M.)). Y.-J.W. acknowledges the Youth Innovation Promotion Association CAS (2021187) and the open research fund of Songshan Lake Materials Laboratory (2023SLABFK13). Y.-T.C. acknowledges the China Postdoctoral Science Foundation (2023M742519). Y.-P.F. and M.-J.Z. acknowledge the Guangdong Basic and Applied Basic Research Foundation (2023A1515011058 (Y.-P.F.), 2022A1515110086 (M.-J.Z.)).

## Acknowledgements

This work is supported by the National Natural Science Foundation of China (U24A2013 (Y.-L.T.), 52122101 (Y.-J.W.), 52471022 (Y.-J.W.), 12504020 (Y.-T.C.), 52501016 (Y.-P.F.), 52401018 (M.-J.Z.), 52202184 (M.-J.H.)), the National Key Research and Development Program of China

## Author contributions

Y.-L.T., Y.-L.Z. and X.-L.M. conceived the project of interfacial characterization in oxides by using aberration-corrected STEM. R.-J.J., Y.-L.T., Y.-L.Z. and X.-L.M. designed the experiments. R.-J.J. performed the thin-film growth and STEM observations. M.-X.Z., D.M., C.H.L. and Y.-J.W. performed the phase-field simulations. S.-Z.L., Y.-T.C., Y.-P.F., M.-J.Z., and M.-J.H. participated in the thin-film growth and STEM observations. D.M. and Y.-J.W. carried out digital analysis of the STEM data. All authors participated in discussion and interpretation of the data.

## Competing interests

The authors declare no competing interests.

## Additional information

**Supplementary information** The online version contains supplementary material available at <https://doi.org/10.1038/s41467-026-70515-y>.

**Correspondence** and requests for materials should be addressed to Yun-Long Tang, Yin-Lian Zhu or Xiu-Liang Ma.

**Peer review information** *Nature Communications* thanks Jaekwang Lee and the other anonymous reviewer(s) for their contribution to the peer review of this work. A peer review file is available.

**Reprints and permissions information** is available at <http://www.nature.com/reprints>

**Publisher's note** Springer Nature remains neutral with regard to jurisdictional claims in published maps and institutional affiliations.

**Open Access** This article is licensed under a Creative Commons Attribution-NonCommercial-NoDerivatives 4.0 International License, which permits any non-commercial use, sharing, distribution and reproduction in any medium or format, as long as you give appropriate credit to the original author(s) and the source, provide a link to the Creative Commons licence, and indicate if you modified the licensed material. You do not have permission under this licence to share adapted material derived from this article or parts of it. The images or other third party material in this article are included in the article's Creative Commons licence, unless indicated otherwise in a credit line to the material. If material is not included in the article's Creative Commons licence and your intended use is not permitted by statutory regulation or exceeds the permitted use, you will need to obtain permission directly from the copyright holder. To view a copy of this licence, visit <http://creativecommons.org/licenses/by-nc-nd/4.0/>.

© The Author(s) 2026